Proceedings of the 2nd International Congress APMAS2012, April 26–29, 2012, Antalya, Turkey

The Use of Sensor Binning Option in Double-Shutter CCD Based Digital Particle Image Velocimetry

B. Akselli[a,*] and İ. Teke[b]

[a]Scientific and Technical Research Council of Turkey-National Metrology Institute
TÜBİTAK-UME, Kocaeli, Turkey

[b]Department of Mechanical Enginnering, Yildiz Technical University, Istanbul, Turkey

In this work we present an experimental investigation of the benefits of double-shutter CCD's pixel binning option in double-frame particle image velocimetry experiments. The CCD binning process increases the sensitivity, signal-to-noise ratio and frame rate of the imaging sensor at the cost of spatial resolution. In order to explore the benefits of the CCD pixel binning option, in low level illuminated particle image velocimetry measurements, we have carried out of series of flow velocity measurements experiments in 30 μm $\times$ 300 μm $\times$ 50000 μm microchannel using micro particle image velocimetry setup. The system is equipped with dual cavity laser system conjugated with an optical attenuator for volume illumination, a double-shutter CCD camera (1392×1040 quadratic pixels with 6.45 μm size), a high magnification optical epifluorescent microscope and a syringe pump. The flow images were recorded at normal, 2×1, 1×2 and 2×2 pixel binning modes of a monochrome CCD camera. A comparison of velocity vector patterns obtained in low level illumination experiments for four different pixel binning modes shows that pixel binning option significantly increases the signal-to-noise ratio in particle image velocimetry recordings. A good agreement of experimental velocity profiles obtained using cross-correlation analysis and sub-pixel interpolation scheme based on a Gaussian regression with theoretical calculated profiles shows the consistency of the experimental results.

DOI: 10.12693/APhysPolA.123.439

PACS: 47.80.Jk

1. Introduction

Particle image velocimetry (PIV), a non-invasive, full field optical measuring technique was introduced about 30 years ago [1] and became a dominant tool for visualisation and velocity measurement of fluid in both macro and micro scales [2–6]. In traditional PIV experiments, the fluid under the investigation is seeded with the tracer particles, which are shining under an excitation by a properly tuned laser light source. The idea behind the method is to precisely register position of corresponding particles in two different instances of time and then from these records ascertain particle displacements. From the overall displacement of particles between two consecutive image frames, the flow velocity can be estimated by Eq. (1.1) [7]:

$$V_{\mathrm{P}} \cong \Delta X_{\mathrm{P}}/(M_0 \Delta t), \tag{1.1}$$

where, ΔX_{P} is the two-dimensional position vector in the image plane, M_0 is the optical magnification of particles in the image plane, Δt is the time between two frames, and V_{P} is the velocity vector of the particle or a particle set.

Micron resolution particle image velocimetry (micro-PIV) [8, 9] is a modification of PIV in order to address the small scales of microfluidic devices. In the micro-PIV systems, the whole volume of the flow is illuminated, where the field of view and depth of focus of the microscope's objective define the measurement volume.

In PIV applications, the upper limit of velocity measurements is bounded by certain system characteristics. The dynamic velocity range (DVR) of the PIV system is determined by the maximum and minimum resolvable particle displacement [10]. The illumination level of excited light and the full frame rate of used camera play key role in defining the dynamic velocity range of the micro-PIV system.

The speed of conventional cameras is defined by the number of generated frames per second i.e. fps. The main components of one frame cycle are the integration time and readout time. The first depends on the illumination level and light sensitivity of the camera. The second depends on the type of charge coupled device (CCD), number of pixels, and its readout mechanism. In CCD sensors, during the exposure time photon-generated carriers (electrons or holes) are accumulated in potential wells. After the exposure the photon generated charges are simultaneously shifted (parallel shift) to the storage wells (generally this process takes a few microseconds), and then the charges row by row (serial shift) are shifted to the sensor output.

Generally, the parallel shift is carried out within a few microseconds, while the serial shift depends on the number of rows and may take tens of milliseconds. In other words, in the interframe cameras the CCD readout time strongly depends on the number of rows.

*corresponding author; e-mail: basak.akselli@tubitak.gov.tr

One of the ways to increase the fps of these cameras is the binning process, which can manipulate the charge readout pattern. Binning is the process of combining multiple pixel charges in both the horizontal and vertical directions into a single larger charge called "binned pixel" or "super pixel". This process is performed by specialized control of the serial and parallel registers in a CCD chip right after the exposure time. A charge of the super pixel is equal to the sum of charges of its underlying pixels. The advantage of CCD binning is that it increases the frame rate but it inversely decreases the spatial resolution of the CCD [5, 11]. Figure 1 shows an example of 2×1 horizontal binning and 1×2 vertical binning mechanism. 2×2 binning mode can be considered as consecutive combining of 1×2 and 2×1 binning modes.

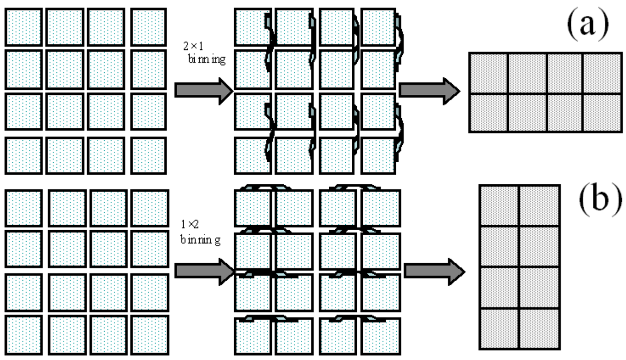

Fig. 1. Schematic presentation of (a) 2×1 horizontal binning, and (b) 1×2 vertical binning mechanisms.

In the CCD binning process, the original image spatial resolution is decreased. On the other hand, frame rate, sensitivity, and signal-to-noise ratio are increased. The benefits of increased frame rate (i.e. DVR of PIV system), due to the binning option, were investigated in author's previous investigations [5, 6, 12]. In these investigations, it was shown that in traditional PIV measurements the binning option can increase at least twice the CCD frame rate, i.e. maximum assessable velocity. However, the impact of binning option of double shutter CCD on the results of double-frame PIV is not yet studied. In the binning modes the signal-to-noise ratio (SNR) can be increased in two ways; firstly by combining charges from all individual pixels being binned together positively influenced the signal level and secondly by reducing the number of charge transfers the readout noise is decreased.

In present investigations, the benefits of employment of CCD binning option (in terms of increased sensitivity and SNR) in double-frame micro-PIV measurements were investigated.

A series of experiments on real microflows inside a microchannel were performed at normal, 1×2, 2×1 and 2×2 CCD binning modes. The results show that at low level illumination micro-PIV experiments, cross-correlation calculations between double-frames are more effective in 1×2, 2×1 and 2×2 binning modes, than at CCD normal mode.

In next section, essentials of the double-shutter CCD camera in the frame of double-frame PIV experiments were briefly described. Section 3 depicts the description of the used experimental setup. In Sect. 4, the measurement results and discussion were presented. Final conclusions were provided in Sect. 5.

2. Double shutter

The frame rate of the CCD depends on some external and internal parameters. Illumination level, spectral content of the emanating light, signal-to-noise ratio, performance of the imaging optics can be listed as some external parameters and spectral quantum efficiency, well capacity are the internal parameters. The integration time of the modern sensors are adjustable between 1 μm to about 1 min or even more. On the other hand, the readout time is a fixed instrumental parameter. For a specific sensor, it depends on the total number of photoactive pixels, digitizer bit depth, sensors type and charge transfer electronics subsystem. The readout time of the most megapixels CCD cameras ranges between 50 to 100 ms. The multiple charge transfers over long distances and the utilization of a single readout node for the charge-to--voltage conversion, is a major restriction for the frame rate of CCD sensors.

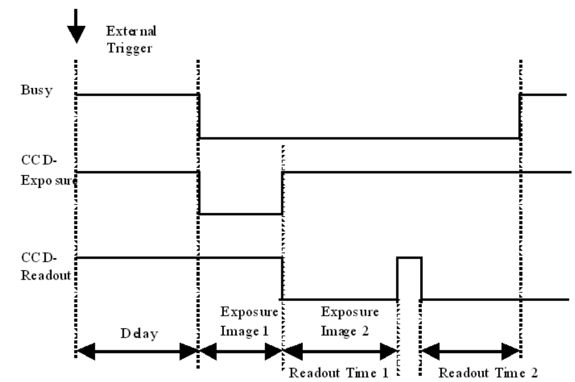

Fig. 2. Schematic presentation of double shutter CCD camera principle.

The use of short duration illumination pulses permits the operation of frame-transfer or interline CCDs in a special mode known as "double-frame" wherein two images can be recorded in very short time interval (a few μs). This type camera is an alternative to high speed cameras. The triggering can be done either internally by the software or by an external trigger signal (Fig. 2). In such cameras, the exposure of the first image is adjustable by the double-shutter mode, but the exposure of the second one is automatically set equal to the sensor readout time. The charge of each pixel after first exposure is immediately transferred to the shielded cells, where these cells act as memory elements. Since the photoactive pixels are empty, they can start capturing the next frame. While the charges of the first frame are being transferred from the cells to the readout node of the sensor, the camera captures the second frame. After the readout process of the first frame and also the exposure of the second frame is stopped, the charges of the second frame are transferred to the output node. During this time, the sensor is photo-inactive. At the end, two separated full frames (double-frames) with a very short interframing time is obtained, as shown in Fig. 1. The interval between a series of double-frames is equal to one readout time order of tens of ms [13, 14].

3. Experimental setup

In the experiments, laminar flows inside of a rectangle microchannel with cross-section 30 μm $\times$ 300 μm and a length 50 mm was investigated. The microchannels were made from borosilicate glass. During the experiments, one end of the microchannel was connected to a syringe pump using rubber tubing, and the other end to a reservoir tank. A programmable syringe pump (NE-1000, New Era Pump Systems, Inc.) is used for driving the flow. The measurements were done at various flow rates, which were adjusted to a desired value by changing the infusion rate of the pump. In the experiments, deionized water was seeded with spherical polystyrene fluorescent microspheres (Duke Scientific, USA). The density of microspheres in the liquid is approximately $\rho = 1.05$ g/cm^3. Flow measurements were performed using 3 μm diameter microspheres, where the volumetric particle concentration was approximately 0.3%. The microspheres had an absorption and emission maxima at 545 nm and 612 nm wavelengths, respectively. For each set of experiments, sufficient time (more than 10 min) was allowed to pass after setting the flow rate and allow the flow to reach a steady state. The PIV measurements were carried out at room temperature, $21.0 \pm 0.5\,^{\circ}$C.

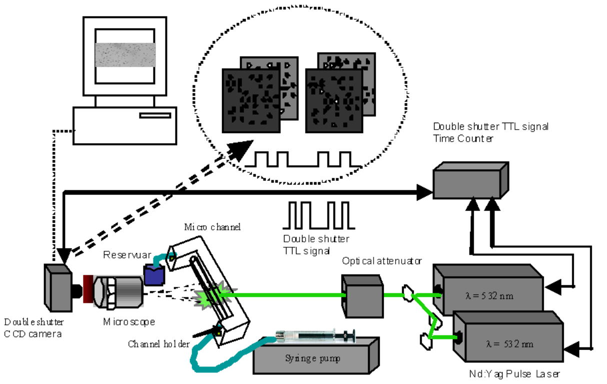

Fig. 3. Experimental setup.

Our micro-PIV system consists of a double cavity Nd:YAG laser system conjugated with an 1–100$\times$ optical attenuator (NL-310 series, Ekspla) with a wavelength of 532 nm, a variable zoom lens (1–10$\times$) conjugated with a microscope objective and a double-shutter CCD camera (PCO Pixelfly). In our experiments, Hirox OL-700II microscope objective was used (Fig. 3). The laser beam was expanded and directed to the coaxial entrance of the microscope, and then focused onto the investigated part of the microchannel. The excited light of the microspheres (filtered out from laser illumination and background light with a long pass color filter) is captured by the double shutter CCD camera through the microscope system. The homemade image recording software was able to record a cycle of PIV images (200 frames) in the normal mode and at the 2×1, 1×2 and 2×2 binning modes. Just after finishing a cycle the captured frames were stored in uncompressed TIFF format to the hard disc storage, thereby avoiding any delay resulting from computer systems.

4. Experimental results and discussions

In this section, we describe our experimental results with the real flow, where effects of various binning modes to the accuracy of micro-PIV measurements were assessed. The micro-PIV experiments were divided into cycles, where each cycle was performed in three stages: (1) beginning stage, where the flow images are captured using normal camera mode, (2) middle stage, where the camera is immediately turned into the desired binning mode for capturing binning images, (3) stopping stage in which the camera is again returned to the normal mode, where flow images again are captured. If the variation of the mean velocities between the beginning and stopping stages was more than 2%, the whole cycle was excluded from further calculations. Sample images are captured

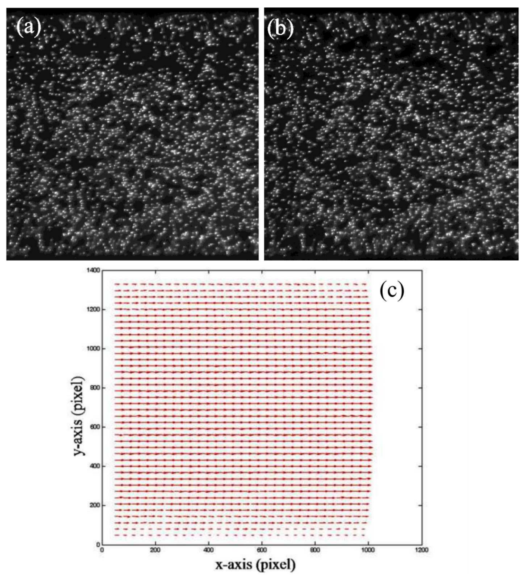

Fig. 4. Double-frame image samples at normal CCD mode ((a) and (b)), corresponding velocity profile (c).

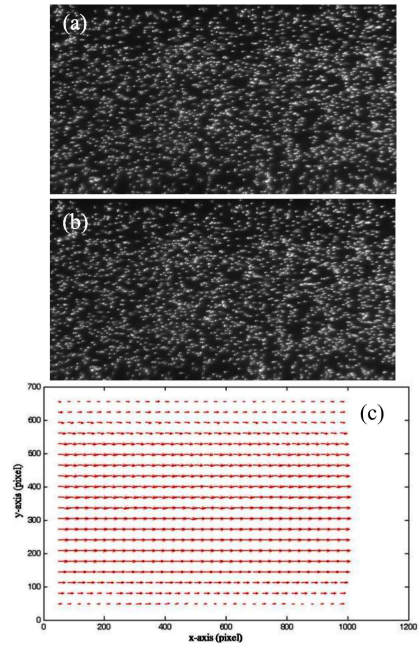

Fig. 5. Double-frame image samples at 2×1 binning mode ((a) and (b)), corresponding velocity profile (c).

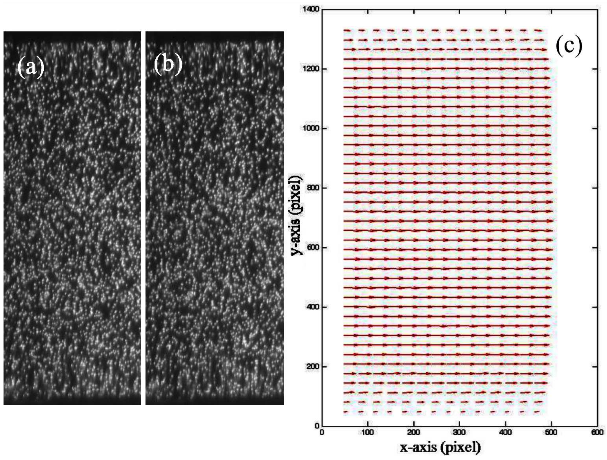

Fig. 6. Double-frame image samples at 1×2 binning mode ((a) and (b)), corresponding velocity profile (c).

at the 1×2, 2×1, 2×2 binning and normal modes during these experiments. Figures 4–7 show the four experimental double-frame images obtained in the microchannel at different pixel binning (PB) modes of the CCD: (a) normal mode (Fig. 4), (b) 2×1 binning mode (Fig. 5), (c) 1×2 binning mode (Fig. 6) and (d) 2×2 binning mode (Fig. 7). The maximum velocity is about 7.8 mm/s and corresponding velocity fields.

These images were captured in the middle section of the microchannel (approximately 15 μm from the wall), where the flow velocity is at its maximum for this configuration of the microchannel (30 μm $\times$ 300 μm).

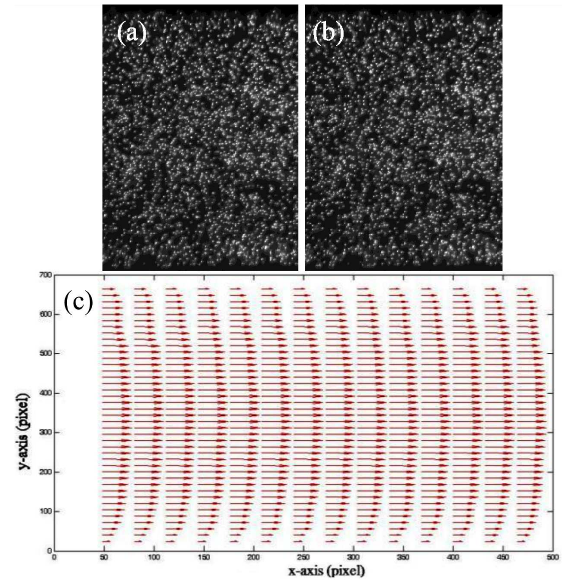

Fig. 7. Double-frame image samples at 2×2 binning mode ((a) and (b)), corresponding velocity profile (c).

The velocity vector profiles were obtained by employing a normalized cross correlation, where, for the best estimate of the particle displacements, a normalized cross-correlation function, defined as follows, was used [15]:

$$C(u,\ v) = \left\{ \sum_{x,y} \left[I(x,y) - \bar{I}(u,v)\right] \times \left[T(x-u,y-v) - \bar{T}(u,v)\right] \right\} \Big/ \left\{ \sqrt{\sum_{x,y} \left[I(x,y) - \bar{I}(u,v)\right]^2} \times \sqrt{\sum_{x,y} \left[T(x-u,y-v) - \bar{T}(u,v)\right]^2} \right\}, \tag{4.1}$$

where $\bar{I}(u,v)$ and $\bar{T}(u,v)$ denote mean values.

Since the peak in normalized cross correlation function (NCFF) is located at a discrete location, which is due to the discrete nature of Eq. (4.1), the displacement calculated using the normalized cross-correlation function is coarse. In order to increase accuracy of distance estimation in PIV, it is necessary to locate the correlation peak within sub-pixel accuracy. A variety of sub-pixel interpolation methods have been proposed in the literature [16, 17]. In Ref. [18] a sub-pixel interpolation method, which accounts for non-axially orientated, elliptically shaped particle images or correlation peaks, is proposed.

The best fit to the circular image shapes obtained by the normal binning image acquisition mode is 2D Gaussian interpolation [5]. In order to estimate sub-pixel displacement, a Gaussian surface is fitted to the local neighborhood around the peak of the correlation function. The maximum of the interpolated Gaussian surface is located at Δx, Δy with respect to the index x_0, y_0 of the correlation peak. Assuming that the correlation peak has a Gaussian-distribution shape, the accurate location of the correlation peak is

$$x = x_0 + \Delta x \quad \text{and} \quad y = y_0 + \Delta y, \tag{4.2}$$

where

$$\Delta x = \frac{\ln C(x_0-1,y_0) - \ln C(x_0+1,y_0)}{\ln C(x_0-1,y_0) + \ln C(x_0+1,y_0) - 2\ln C(x_0,y_0)} \tag{4.3}$$

and

$$\Delta y = \frac{\ln C(x_0,y_0-1) - \ln C(x_0,y_0+1)}{\ln C(x_0,y_0-1) + \ln C(x_0,y_0+1) - 2\ln C(x_0,y_0)} \tag{4.4}$$

As noted in [6] any asymmetric binning mode introduces scale distortion to the output image. Any distortion in the image acquisition step, which does not affect the particle location information, can be overcome by determining the nature of this distortion and applying corresponding corrections.

At the vertical 2×1 binning mode the particle images and corresponding correlation peaks are oriented along the x axis and are deformed (by a 1:2 ratio). By applying two-dimensional regression, it can be shown that the sub--pixel location of the peak is reformulated as

$$x = x_0 + \Delta x \quad \text{and} \quad y = y_0 + \Delta y/2, \tag{4.5}$$

where Δx and Δy are defined as in Eqs. (3) and (4), respectively [6, 12].

In a similar way, for the horizontal, 1×2 binning mode, where particle images and corresponding correlation peaks are oriented along the x axis and are deformed (by a 2:1 ratio), the sub-pixel location of the peak is reformulated as

$$x = x_0 + \Delta x/2 \quad \text{and} \quad y = y_0 + \Delta y. \tag{4.6}$$

The velocity fields for each investigated binning modes calculated by this way are shown in Figs. 4–7c. The size of the interrogation windows were 128×64 for normal mode, 64×32 for 2×2 binning mode, and 64×64 and 128×32 for 1×2 and 2×1 binning modes, respectively. We analyzed more than 50 pairs of images and recorded at all binning modes. The statistical analysis of cross--correlation calculations of images obtained at normal mode of the CCD has shown that the number of valid velocity vectors formed about 80% of total number of calculated velocity profiles. This value is increased for the 1×2 and 2×1 binning mode images, obtained at the same illumination level. For these two binning mode, the ratio of valid vectors to the calculated total number of vectors is increased up to 90% and 92%, respectively.

Finally, we have obtained the value for the ratio of 95–96% for the 2×2 binning mode. These results depicts that the CCD binning option can be used to increase the PIV image quality in most low illumination conditions.

We compared the experimental velocity profiles with

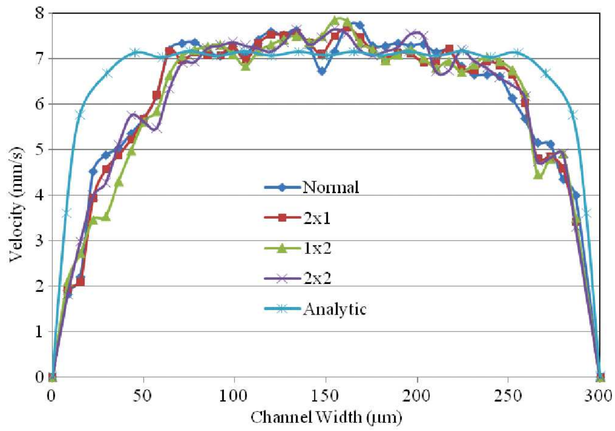

Fig. 8. Velocity profiles for four different binning modes and analytically calculated results.

a theoretically calculated profile to verify the reliability of obtained results. The analytical velocity profile for rectangular cross-section in Fig. 8 was obtained using the following equations [19]:

$$u(y,z) = \frac{16a^2}{\mu\pi^3}\left(-\frac{\mathrm{d}p}{\mathrm{d}x}\right) \times \sum_{i=1,3,5,\ldots}^{\infty} (-1)^{(i-1)/2}\left[1 - \frac{\cosh(i\pi z/2a)}{\cosh(i\pi b/2a)}\right] \times \frac{\cos(i\pi y/2a)}{i^3} \tag{4.7}$$

$$Q = \frac{4ba^3}{3\mu}\left(-\frac{\mathrm{d}p}{\mathrm{d}x}\right) \times \left[1 - \frac{192a}{\pi^5 b}\sum_{i=1,3,5,\ldots}^{\infty}\frac{\tanh(i\pi b/2a)}{i^5}\right], \tag{4.8}$$

where Q is flow rate, a and b is the dimensions of the cross-section of a channel, μ is a kinematic viscosity.

5. Conclusions

The uncertainty components for PIV and micro-PIV are identical except the components for the different illumination techniques which are sheet for PIV and volume for micro-PIV. The definition of the field depth is the major source of the error in micro-PIV measurements. In literature there are several different definitions of field depth. For the present investigations, the following equation [20] from the literature was used:

$$\Delta z_m = \frac{3n\lambda}{(\mathrm{NA})^2} + \frac{2.16 d_p}{\tan\theta} + d_p, \tag{5.1}$$

where n is the refractive index of the medium and NA is the numerical aperture of the objective lens. For the present measurements, the field depth, according to Eq. (5.1), is equal to 4.8 μm. This implies that the intensity contribution of the particles out of this focus depth has no important influence on the correlation function.

Interrogation volumes in the flow coordinates were the same for all binning modes and equal to 23.25 μm $\times$ 5.8 μm $\times$ 4.8 μm. The interrogation spots were overlapped by 50% to satisfy the Nyquist sampling criterion, which corresponds to 2.7 μm vector-to-vector spacing in the stream-wise-normal direction.

In the normal mode, 3 μm particle was resolved by approximately 4 pixels, which is in accord with the minimum requirement (4–6 pixels). In the binning modes, these values are about 2–3 pixels, which is still recommended in papers [21]. This is essential to obtain the location of a particle image correlation peak to within one tenth of the particle's image diameter [21].

The error contribution due to particle diffusion caused by Brownian motion along the x-axis is given by [21]:

$$\varepsilon_{\mathrm{B}} = \sqrt{2D/(u^2\Delta t)}, \tag{5.2}$$

where D is the Brownian diffusion coefficient

$$D = \frac{kT}{3\pi\mu d_p}. \tag{5.3}$$

In Eq. (5.2), k is Boltzmann's constant and equal to 1.38×10^{-23} J/K, T denotes fluid temperature, d_p is the particle diameter, and μ is the dynamic viscosity of the fluid. For the present investigations with characteristic flow velocity of $u \approx 7.8$ mm/s and $\Delta t = 0.001$ s, this approximately yields to a relative error less than 0.5%.

The system's stability, including the syringe drive pump, was estimated using the standard deviation of calculated mean velocities using the central part of the velocity profiles of different PIV measurement cycles. The stability was found to be within 2% of the maximum mean velocity of the normal mode.

A good agreement between uncertainty parameters calculated for our experimental conditions and those reported in the existing literature indicates the validity of the experiments.

References

[1] R.J. Adrian, *Experim. Fluids* **39**, 159 (2005).

[2] C.E. Willert, M. Gharib, *Experim. Fluids* **10**, 181 (1991).

[3] R.D. Keane, R.J. Adrian, Y. Zhang, *Meas. Sci. Technol.* **6**, 754 (1995).

[4] R.J. Adrian, *Annu. Rev. Fluid Mech.* **23**, 261 (1991).

[5] B. Akselli, A. Kholmatov, H. Nasibov, in: *Int. Symp. on Optomechatronic Technologies*, IEEEXplore, 2009, p. 223.

[6] H. Nasibov, A. Kholmatov, B. Akselli, A. Nasibov, S. Baytaroglu, *IEEE/ASME Trans. Mechatron.* **15**, 527 (2010).

[7] C.D. Meinhart, S.T. Wereley, *Meas. Sci. Technol.* **14**, 1047 (2003).

[8] J.G. Santiago, S.T. Wereley, C.D. Meinhart, D.J. Beebe, R.J. Adrian, *Experim. Fluids* **25**, 316 (1998).

[9] S. Devasenathipathy, J.G. Santiago, S.T. Wereley, C.D. Meinhart, K. Takehara, *Experim. Fluids* **34**, 504 (2003).

[10] R.J. Adrian, *Meas. Sci. Technol.* **8**, 1393 (1997).

[11] A. Kholmatov, B. Akselli, A. Nasibov, H. Nasibov, *Proc. SPIE* **7723**, 77231R-1, (2010).

[12] B. Akselli, I. Teke, *Int. J. Metrol. Qual. Eng.* **2**, 83 (2011).

[13] E. Balaban, A. Nasibov, A. Kholmatov, H. Nasibov, F. Hacizade, *Proc. SPIE* **8430**, 84301I-1 (2012).

[14] Y.H. Li, C.Y. Wu, B.C. Chen, Y.C. Chao, *Meas. Sci. Technol.* **19**, 045401 (2008).

[15] M.R. Cholemari, *Exp. Fluids* **42**, 913 (2007).

[16] H. Nobach, N. Damaschke, C. Tropea, *Experim. Fluids* **39**, 299 (2005).

[17] H. Nobach, M. Honkanen, *Experim. Fluids* **38**, 511 (2005).

[18] M. Raffel, C.E. Willert, S.T. Wereley, J. Kompenhans, *Particle Image Velocimetry — A Practical Guide*, Springer, 2nd ed., 2007.

[19] F.M. White, *Viscous Fluid Flow*, 3rd ed., McGraw Hill, Singapore 2006.

[20] C.D. Meinhart, S.T. Wereley, M.H.B. Gray, *Meas. Sci. Technol.* **11**, 809 (2000).

[21] M.G. Olsen, C.J. Bourdon, *J. Fluids Eng. (Trans. ASME)* **125**, 895 (2003).